Journal of Reinforced Plastics and Composites. May 2021.
doi:10.1177/07316844211020115

Infill pattern and density effects on the bending stiffness of additively manufactured short fibre reinforced polymer sandwich specimens: experimental investigation and finite element analysis

Luca Michele Martulli[1], Pablo Barriga Ruiz[1], Akshay Rajan[1], František Bárnik [2], Milan Sága [2], Andrea Bernasconi [1]*

[1] Politecnico di Milano, Dipartimento di Meccanica, Via La Masa 1, 20156 Milano, Italy

[2] University of Žilina, Faculty of Mechanical Engineering, Univerzitná 8215/1, 01026 Žilina, Slovakia

*Corresponding author: andrea.bernasconi@polimi.it

Abstract

Additively manufactured polymer parts are often designed like composite sandwich structures. In this work, sandwich beam-like specimens with hexagonal, triangular and rectangular infills were manufactured with different infill densities. An influence of the shape of the infill on the overall stiffness was observed. The bending stiffness of the hexagonal specimens was between 13% and 25% lower than that of the other two cases, that, instead, showed similar performances. Numerical simulations were performed using both shell and solid elements for the infill, to check if it was possible to model the differences observed experimentally. All simulations lead to accurate bending stiffness predictions, except for the rectangular infills with higher infill densities, for which overprediction between 20% and 25% was obtained. Based on these results, strategies for the finite element analysis of additively manufactured composite structures are discussed.

Keywords: 3D printed; Sandwich Structures; Finite element analysis (FEA); Mechanical testing; Thermoplastic resin; Elastic performance; Stiffness

1 Introduction

Additive manufacturing or 3D printing technology is a manufacturing process based on a layer-by-layer deposition of fused filaments. These manufacturing technologies allow for faster and cheaper manufacturing of product designs that are difficult to produce with traditional processes [1,2].

Fused Filament Fabrication (FFF), also known as Fused deposition modelling, is one of the most used additive manufacturing technique for polymers [3].Thermoplastic filaments are extruded and deposited layer-by-layer into the final part. Since the polymer is heated only 1 °C above its melting temperature [1], it solidifies immediately after deposition. Several studies investigated the effects of layer thickness, orientation, raster angle, filament width and air gaps on the tensile, flexural and impact performance on 3D printed polymers (many of them are gathered in the review paper of Dizon et al. [4]). It was highlighted that the variation of these parameters does not always imply a direct increase or decrease of material performance; instead, several conflicting factors exist, making it difficult to predict the performance variation based on a parameter variation. Generally, the printed material is anisotropic, with the best mechanical performance achieved along the printing direction: it is thus advisable to choose a raster angle that ensures an alignment between the deposited filaments and the local principal stresses [5–10].

A recent development of FFF is the printing of thermoplastic polymers reinforced with short fibres [9,11–18]. Both glass [9,11,18] and carbon fibres [12–16,18] were found to significantly improve the tensile modulus and strength of the material compared to the neat polymer. The

tendency of the fibres to align along the printing direction makes reinforced 3D printed composites even more anisotropic than their unreinforced counterparts [12,18].

FFF parts and specimens are often designed as sandwich-like structures, with an internal core or infill surrounded by a contour shell and upper and lower skins. The shape and the density of the infill pattern are important printing parameters that can significantly affect the mechanical performance [9]. Almost all the aforementioned works simply consider a 100% infill. While such specimens allow a deeper material characterisation, they are far from real 3D printed structures, and do not allow to assess the impact of the shape and the density of the infill on the mechanical performance. Carneiro et al. [9] manufactured PP specimens with 20%, 60% and 100% infill density and tested them under tensile loading. Differences of more than 250% in both modulus and strength were observed between the 20% and 100% case. Interestingly, the variation of both properties with the infill density could be fit by a linear regression; the infill density having a linear effect on the tensile properties of the specimens. Naranjo-Lozada et al. [16] manufactured and tested specimens with rectangular (alternating layers at ±45° with respect to load direction) and triangular (filaments at 0° or 60° with respect to load direction, forming triangular cells) infills; 10% and 70% infill were considered for each shape. Moreover, nylon and Onyx, a short carbon fibres reinforced nylon developed by Markforged [19], were used. In all cases, the specimens with triangular shaped infill were significantly stiffer and stronger than their rectangular counterparts: this was attributed to a higher presence of filaments oriented along the load direction. The denser infills also lead to higher tensile properties: the effect was more important for the neat nylon than for the reinforced material, and for the triangular pattern than the rectangular one. Overall, the triangular pattern was suggested as the best choice when dealing with tensile loads. Fernande-Vicente et al. [20] used ABS to produce specimens with rectangular, hexagonal and *line* (a random infill pattern with linear connections between walls) patterns; infill densities of 20%, 50% and 100% were considered. The hexagonal pattern showed higher tensile strength and modulus than the other two at 20% and 50% infills,

and the linear pattern was stiffer and stronger than the rectangular. At 100% infill, however, the rectangular pattern was the best performer, although the differences were small. For all patterns, the infill density had a significantly higher impact than the pattern shape. Finally, Li and Wang [21] manufactured sandwich specimens with 3D printed core materials and tested them under three-points bending. The flexural stiffness, strength and energy absorption of three different core topology: truss, standard honeycomb and re-entrant honeycomb. While the truss pattern showed higher stiffness and strength, the re-entrant honeycomb exhibit higher energy absorption. Numerical simulations were conducted, showing good agreement with experimental data.

Works investigating the effects of the infill on 3D printed specimens are thus scarce and limited to tensile characterisation, or part of a larger investigation. This work aims to assess the effects of the infill shape and density on the flexural elastic properties of 3D printed Onyx specimens, designed like sandwich panels. It is well known that in sandwich beams and panels the core plays a non-negligible role on the overall transverse displacement under the action of transverse loads. Although the bending stiffness is mainly governed by the properties of the skins and the distance between them, the contribution of the shear deformation of the core (the infill) to the overall flexural displacements cannot be disregarded [21,22]. In this work, three different infill shapes are considered, as well as three different infill parameters for each shape, to assess the contribution of the infill to the flexural stiffness of sandwich beam-like specimens. Moreover, Finite Element (FE) simulations are performed to tentatively predict the elastic performance of the specimens and check the performances of different modelling strategies.

Part of the available modelling works is dedicated to the prediction of the properties of the final composite material through homogenisation of the constituents [23,24]. While such models are suitable for structural analysis at the micro and meso-scale, they cannot be used for performance prediction of macro structures and components.

To cope with such limitations, other works [7,25] proposed to use Classical Laminate Theory (CLT) to predict the stiffness of 3D printed parts. This approach is used in this work for the skins and the contour of the specimens. The use of CLT, however, requires the knowledge of more elastic constants than those provided by the supplier. Therefore, 100% infill densities tensile tests specimens were manufactured and tested with different raster angles to back-calculate the said constants. Finally, for the FE model of the infill, both shell and solid elements were considered. The overall objective is to assess the accuracy of these modelling techniques for the prediction of the influence of the infill in the specimens' flexural behaviour.

2 Materials & methods

2.1 Specimens manufacturing

All test specimens were created using FFF additive technology on a Mark Two® printer, using Onyx, a micro carbon fibre filled polyamide. In all cases, the layer height and filament width were 0.2 mm and 0.4 mm, respectively.

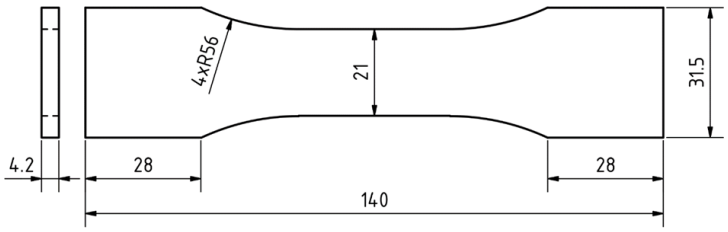

Fig. 1: Geometry of the 0°/90° specimens

2.1.1 Tensile tests specimens

Tensile tests were first performed to back-calculate the anisotropic properties of the Onyx deposed filament. The specimens consist of two concentric rings as contour, and a 100% infill. Two different printing orientations were considered for the infill: three rectangular specimens, of dimension 200 mm x 30 mm x 6 mm, were manufactured with an alternate orientation of

±45°; three dog-bone specimens, whose dimensions are reported in Fig. 1, were manufactured with an alternate orientation of 0°/90°.

2.1.2 Three points bending specimens

The three points bending specimens are composed of two skin layers, a contour shell and the infill (see Fig. 2). Their dimensions are 120 mm x 30 mm x 6 mm. For all specimens, the upper and lower skins consist of 4 layers printed with alternate orientations of ±45°. The contour shell is made of two concentric rings.

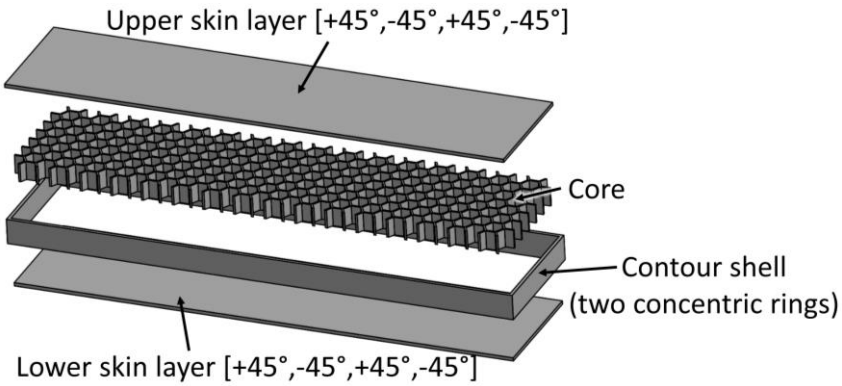

Fig. 2: Schematic of the sandwich structure composing the three points bending specimens (not to scale).

Three different shapes were considered for the infill patterns: hexagonal, triangular and rectangular; moreover, three different print densities (40%, 60%, 80%) were selected for each shape on the Eiger software, the proprietary software of the Markforged printers that defines the manufacturing process. In the rest of the paper, the three points bending specimens will be referred to with the first capital letter of the infill shape (H for hexagonal, T for triangular and R for rectangular) followed by the infill density. The considered patterns are shown in Table 1.

Journal of Reinforced Plastics and Composites. May 2021.
doi:10.1177/07316844211020115

Table 1: Infill patterns of the three points bending tests. The images shown are the ones generated by the 3D printer's proprietary software Eiger. For visibility reasons, only half of the specimens is shown. Note that the rectangular pattern is made of layers having an alternate orientation of ±45°: the figures in the table show only one layer with a single orientation.

	40%	60%	80%
Hexagonal	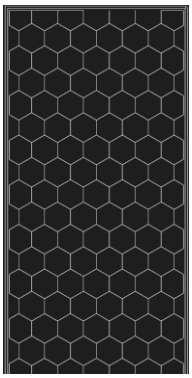		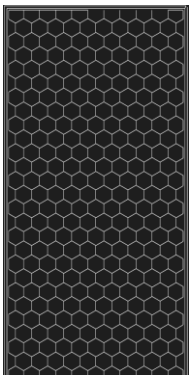
Triangular	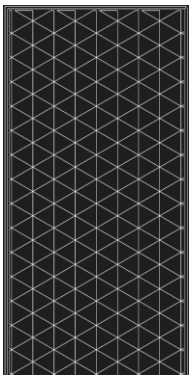	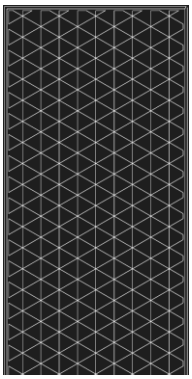	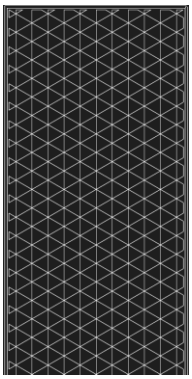
Rectangular			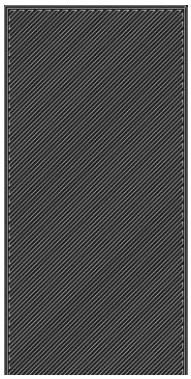

2.2 Mechanical testing

The quasi-static tensile tests were performed according to the ISO 524-4 standard [26]. An MTS Alliance RT100 machine was used, equipped with an additional 1.5 kN load cell, at a 0.5 mm/s loading rate. 2D Digital Image Correlation (DIC) was used to measure the surface strain on one side of the specimens; to this end, a random speckle pattern was applied with spray paint on the analysed surfaces. The images were analysed with the GOM Correlate software. The Young's modulus was calculated in the longitudinal strain range of 0.05% and 0.25%, as suggested by the standard [26]. Three specimens per type were tested (for a total of six).

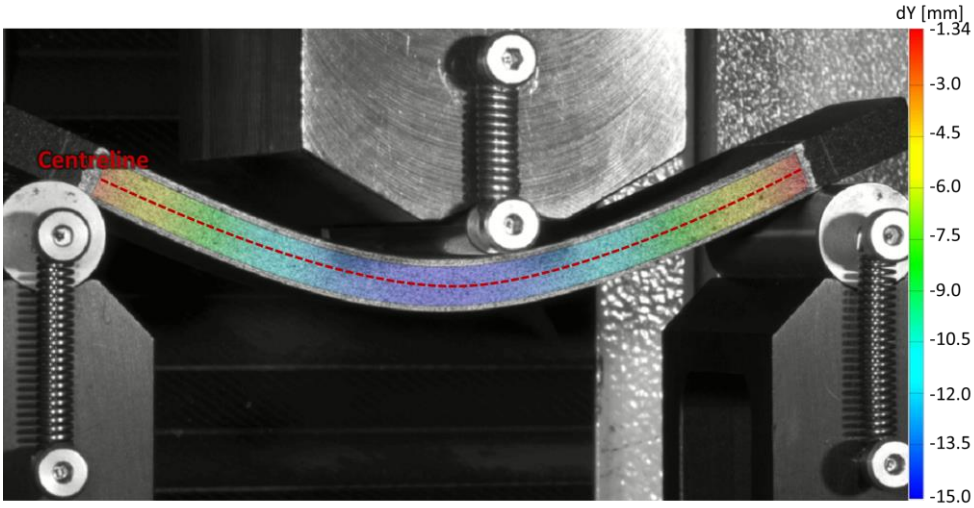

Fig. 3: DIC image: vertical displacement of a tested specimen.

The three points bending tests were performed according to the ISO 178 standard [27]. An MTS Acumen test machine was used, featuring a 1 kN load cell, at a 5 mm/min. load rate. The span between the supports was 96 mm. A 3D DIC ARAMIS adjustable system was set up to measure the specimen's deflection during the tests. To this purpose, a random speckle pattern was applied with spray paint on one side surface of the specimens. The images were analysed with the GOM Correlate software: the vertical displacement of the centreline of the analyse surface was extracted (see Fig. 3); the point of this line with the highest absolute displacement was used

to calculate the bending stiffness of the specimens. This was evaluated with reference to the load range that corresponded to longitudinal strain values in the top and bottom layer of 0.05% and 0.25%, according to the standard [27]. Three specimens per type were tested (for a total of 27).

3 Results of the tests and discussion

3.1 Tensile tests result and extraction of elastic constants

Table 2 shows the results of the quasi-static tensile tests in terms of longitudinal Young's modulus and Poisson's ratio. Values of Young's modulus for 3D printed short carbon fibre reinforced polymers with [0/90] orientation higher than the [±45] case are also reported in [15].

Table 2: Tensile tests results. ± denotes standard deviation

Specimens	**±45°**	**0°/90°**
Young's modulus (MPa)	642 ± 82	1159 ± 31
Poisson's ratio	0.66 ± 0.02	0.25 ± 0.01

An accurate modelling of the sandwich-like structures tested in bending conditions requires the knowledge of the engineering constants of the Onyx filament, i.e of the 3D printed material along the deposition path. These constants can be calculated from the tensile tests results using CLT. This approach relies on the assumption that the 3D printed specimens with 100% infill and different raster angles behave like a composite laminate.

From CLT, the resultant force vector **N** and moment vector **M** applied to a composite structure relate to strain vector **ε** and curvature vector **K** as [28]:

$$\begin{bmatrix} \boldsymbol{N} \\ \boldsymbol{M} \end{bmatrix} = \begin{bmatrix} \boldsymbol{A} & \boldsymbol{B} \\ \boldsymbol{B} & \boldsymbol{D} \end{bmatrix} \begin{Bmatrix} \boldsymbol{\varepsilon} \\ \boldsymbol{K} \end{Bmatrix} \quad \textbf{(1)}$$

For the definition of the matrices **A**, **B** and **D**, the reader is referred to [28]. The printing orientations of the layers can be represented by the following stacking sequences: $[(45/-45)_{15}]$ and $[(0/90)_{15}]$. Since these stacking sequences are quasi-symmetric, the terms A_{13}, A_{23}, A_{31} and A_{32} of the **A** matrix and all the terms of the **B** matrix are assumed to be negligible. Under these assumptions, applied moments **M** and curvatures **K** are zero during a tensile test. Therefore, (1 specialised to the tensile tests case can be written as:

$$\begin{bmatrix} \boldsymbol{N_x} \\ \boldsymbol{N_y} \\ \boldsymbol{N_{xy}} \end{bmatrix} = \begin{bmatrix} \boldsymbol{A_{11}} & \boldsymbol{A_{12}} & \boldsymbol{0} \\ \boldsymbol{A_{12}} & \boldsymbol{A_{22}} & \boldsymbol{0} \\ \boldsymbol{0} & \boldsymbol{0} & \boldsymbol{A_{33}} \end{bmatrix} \begin{Bmatrix} \boldsymbol{\varepsilon_x} \\ \boldsymbol{\varepsilon_y} \\ \boldsymbol{\gamma_{xy}} \end{Bmatrix} \quad \textbf{(2)}$$

which further becomes:

$$\boldsymbol{N_x} = \left(\boldsymbol{A_{11}} - \frac{\boldsymbol{A_{21}^2}}{\boldsymbol{A_{22}}} \right) \boldsymbol{\varepsilon_x} \quad \textbf{(3)}$$

The Young's modulus of the laminate can thus be estimated as:

$$E_{x-est} = \frac{1}{h} \left(\boldsymbol{A_{11}} - \frac{\boldsymbol{A_{21}^2}}{\boldsymbol{A_{22}}} \right)$$

with *h* being the thickness of the specimen.

Similarly, the Poisson's ratio can be estimated as:

$$\nu_{xy-est} = \frac{A_{12}}{A_{22}}$$

To obtain the engineering constants of the Onyx filament, an iterative procedure is used. The procedure is set to minimise the sum of the relative error [29,30]:

$$f_{obj} = \left(\frac{E_{x-est} - E_{x-exp}}{E_{x-exp}}\right)_{0/90}^{2} + \left(\frac{E_{x-est} - E_{x-exp}}{E_{x-exp}}\right)_{\pm 45}^{2} + \left(\frac{\nu_{xy-est} - \nu_{xy-exp}}{\nu_{xy-exp}}\right)_{0/90}^{2} + \left(\frac{\nu_{xy-est} - \nu_{xy-exp}}{\nu_{xy-exp}}\right)_{\pm 45}^{2}$$

where the subscripts "est" and "exp" refers to the estimated and experimental values, respectively, and the subscripts 0/90 and ±45 refers to the 0/90 and ±45 tests, respectively. The solver employs a generalized reduced gradient technique for the optimisation. The initial guesses of the procedure are shown in Table 3. The procedure first evaluated the optimised values of E_{11} and E_{22}, while G_{12} and ν_{12} were kept constant; then, the opposite was done: with the new optimised values of the moduli kept constant, G_{12} and ν_{12} were allowed to change. A condition was imposed for the Poisson's ratio ν_{12} to be smaller than 1.

The supplier's datasheet for the Onyx material [19] reports a longitudinal modulus E_{11} of 2400 MPa. The value obtained with the iterative solution differs by 45% with respect to this value. The difference could be ascribed to the use of tests plaques that are reported as uniquely designed to maximize test performance [19], whereas the tests reported herein are more representative of the actual printing process of the sandwich specimens tested in this work.

Table 3: Results of the iterative procedure

Engineering constant	Initial guess	Converged values
E_{11} (MPa)	2400	1322
E_{22} (MPa)	750	1016
G_{12} (MPa)	380	190
υ_{12}	0.4	0.29

3.2 Three points bending specimens and tests

Table 4 reports the volumes of the different infills. The infill relative density, as the ratio between said volume and the total internal volume of the specimen (118.4 mm x 28.4 mm x 4.4 mm), is also reported in brackets. It must be pointed out that the Eiger software settings (40%, 60% and 80%) do not correspond to an absolute value of the volume fraction and are to be understood as proprietary settings. Nevertheless, the notation will be kept throughout this article for the sake of simplicity of specimens' identification.

Table 4: Volume occupied by the different infills. The quantities in brackets indicate the fraction of this volume to the available internal volume (relative volumetric density).

	Hexagonal	**Triangular**	**Rectangular**
40 %	2680 mm^3 (18.1 %)	4746 mm^3 (32.1 %)	8230 mm^3 (55.6 %)
60 %	3393 mm^3 (22.9 %)	5159 mm^3 (34.9 %)	11594 mm^3 (78.4 %)
80 %	4525 mm^3 (30.6 %)	5819 mm^3 (39.3 %)	13942 mm^3 (94.2 %)

Table 5 reports the measured specimens' stiffness during the three points bending tests. The maximum difference is observed between the H40 (least rigid) and T80 (most rigid) specimens: such difference is about 30% of the T80 stiffness. Although smaller than the contribution of the skin layers, the effect of the infills on the bending stiffness of the specimens is clearly not negligible.

As shown, the hexagonal pattern is the least rigid of the three shapes considered; this is likely due to the low relative volumetric densities of the hexagonal pattern, the lowest ones of the three patterns considered. The low relative volumetric density also implies a larger size of the hexagonal cells, which are thus more deformable in shear. On the other hand, the hexagonal pattern performed better than the rectangular one in [20]; where unreinforced ABS was used as

printing material. To the best of our knowledge, no work verified if this applies also for unreinforced Nylon. If that would be the case, the stiffness increase due to the addition of the fibres might thus not be equal for all the patterns: the fibres might thus reinforce less effectively the hexagonal pattern than the rectangular. Given its larger cell size, the hexagonal pattern indeed has fewer walls oriented along the stress direction, while the other two walls are oriented at ±60°, as schematically depicted in Fig. 4a. Moreover, these walls oriented along the stress direction are discontinuous.

Table 5: Three points bending results in terms of specimens' stiffness. ± denotes standard deviation. The quantities in brackets indicate the variation with respect to the previous infill parameter (considering the same infill pattern's shape)

	Hexagonal	**Triangular**	**Rectangular**
40 %	12.4 ± 0.8 N/mm -	15.7 ± 0.9 N/mm -	15.3 ± 2.9 N/mm -
60 %	13.8 ± 0.9 N/mm (+ 11.3 %)	16.6 ± 1.3 N/mm (+ 5.7%)	16.4 ± 1.8 N/mm (+ 7.2 %)
80 %	15.6 ± 1 N/mm (+ 13%)	17.4 ± 1.9 N/mm (+ 4.8 %)	17.2 ± 1.4 N/mm (+ 4.9 %)

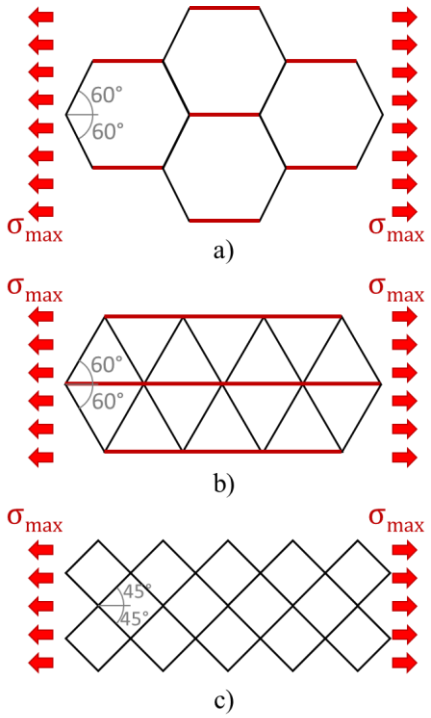

Fig. 4: Orientation of the a) hexagonal, b) triangular and c) rectangular patterns with respect to the maximum stress direction. The walls in red are those with a favourable orientation.

This is not the case for the triangular pattern, that outperforms the other cases. The triangular pattern was also found to outperform the rectangular ones in tensile conditions in [16] for Onyx specimens. These results are likely due to the presence of the continuous walls oriented along the stress direction, which is the same in both tension and bending (see Fig. 4b). Given the higher relative volumetric density, the occurrence of these favourably oriented walls is also higher than the hexagonal case.

Finally, the rectangular pattern showed rigidities higher than the hexagonal ones too. Although this pattern does not have walls oriented along the stress direction, it has a significantly higher relative volumetric density than all other patterns. The cells are thus very small, and in spite of the walls oriented at ±45°, the pattern displays high stiffness (see Fig. 4c). However, the rectangular patterns' rigidities are consistently smaller than the triangular ones, which have smaller relative volumetric density. The relative volumetric density does not thus play a paramount role in the stiffness determination but is rather one of the contributing factors.

It is possible to fit the data for each infill shape by a linear regression with R^2 values of 0.9949, 0.9997 and 0.9883 for the hexagonal, triangular, and rectangular patterns, respectively. Such good fit suggests that the effect of the infill density parameter on the flexural stiffness of the specimens might be linear, as observed for the tensile modulus in [9].

Table 5 also reports the stiffness increase due to the infill parameter increase. While showing less performance, the hexagonal pattern showed a significantly higher sensibility to the infill parameter.

4 Fnite element modelling

4.1 Preprocessing

The bending tests were simulated using the FE Abaqus software by Simulia. Only one quarter of the specimen was simulated thanks to the double symmetry of the specimens. For all simulations, the skins and the sidewalls were modelled as composite laminates, using the dedicated tool implemented in Abaqus, with a $[(45/-45)_2]$ and a $[(0)_2]$ stacking sequence, respectively. Skins and sidewalls all constituted a single part, defined as the outer shell (shown in Fig. 5), which was meshed with solid elements with an average element length of 1 mm. The material properties considered for a 0° unidirectional lamina (sidewalls) are the ones reported in Table 3, considering $E_{33}=E_{22}$, $G_{13}=G_{23}=G_{12}$ and $\nu_{13}= \nu_{23}= \nu_{12}$.

For the infill, two different simulations were performed, using either shell or solid elements, to evaluate the performance of each modelling strategy. The nodes of the outer boundaries of the infill were constrained kinematically to the ones of the solid elements at the inner surfaces of the outer shell (TIE constraint according to Abaqus nomenclature). The support was simulated by preventing any vertical displacement along the nominal contact line between the supporting cylinder and the lower skin; the loading cylinder was simulated by imposing a 1 mm vertical displacement along the nominal contact line between the loading cylinder and the upper skin. These boundary conditions are shown in Fig. 5. Symmetry was imposed by preventing X-axis

displacement and Y-axis and Z-axis rotation on the YZ plane, and Z-axis displacement and X-axis and Y-axis rotation on the XY plane.

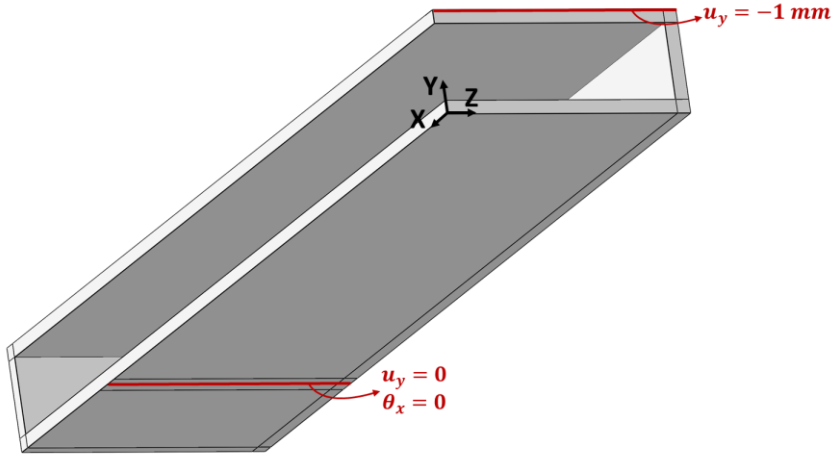

Fig. 5: View of the outer shell model and the applied boundary conditions (excluding symmetric ones)

The different infills geometry were defined by analysing the images produced by Eiger reported in Table 1. The images are analysed with ImageJ [31] to measure accurately:

- the edge length of a hexagonal cell;
- the edge of a triangular cell (all triangles of the pattern are equilateral);
- for the rectangular pattern, the distance between the filaments.

The thickness of the cells' walls is 0.4 mm, equal to the width of the filament. With these dimensions it was possible to reconstruct the different patterns of the infill. For example, Fig. 6 showcases the H60 infill, modelled with shell (a) and solid (b) elements.

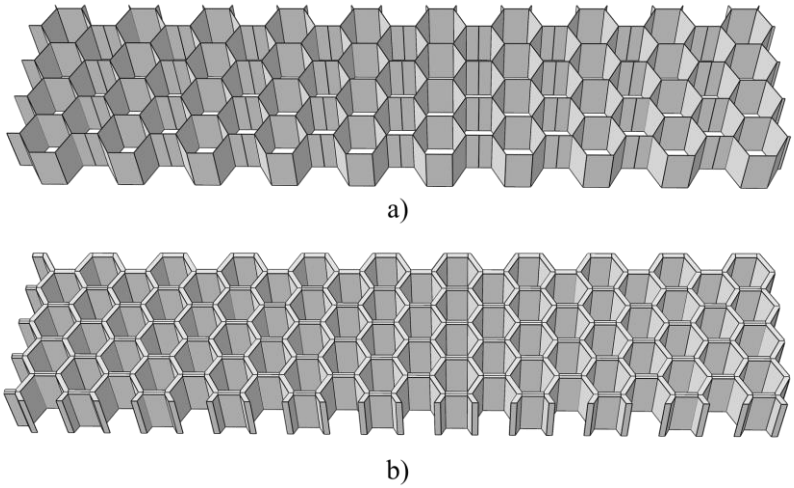

Fig. 6: a) Shell and b) solid model of the H60 infill

However, by this method it was not possible to reconstruct the R80 pattern, because the distance between the filaments, in the images produced by Eiger, was smaller than half the filament thickness. This would have made it physically impossible for the printer to obtain such pattern. An R80 specimen was thus cut to observe the infill and understand the printer strategy to achieve the 80% infill; the same was done to a R40 specimen for comparison. The micrographs are shown in Fig. 7, and compared (at the same scale) with the Eiger images used for setting their manufacturing process. Fig. 7a shows a good correlation between the Eiger image and the actual printed pattern for the R40 specimen; however, Fig. 7b shows significant difference between the Eiger image and the actual printed infill. As mentioned before, it was physically impossible for the printer to follow the equally spaced filaments pattern of the Eiger software; it appears that, to ensure the 80% filling, the printer deposited filaments at two alternating distances. As a result, the R80 pattern is made of a sort of double filament composing the rectangular pattern (see Fig. 7b).

For the R80 specimens only, the infill modelled with solid elements was defined considering the dimensions measured from the micrograph in Fig. 7b (ImageJ is used). Two simulations were

performed with shell elements, the first considering the nominal dimensions from the Eiger images and the second the actual ones from the micrograph.

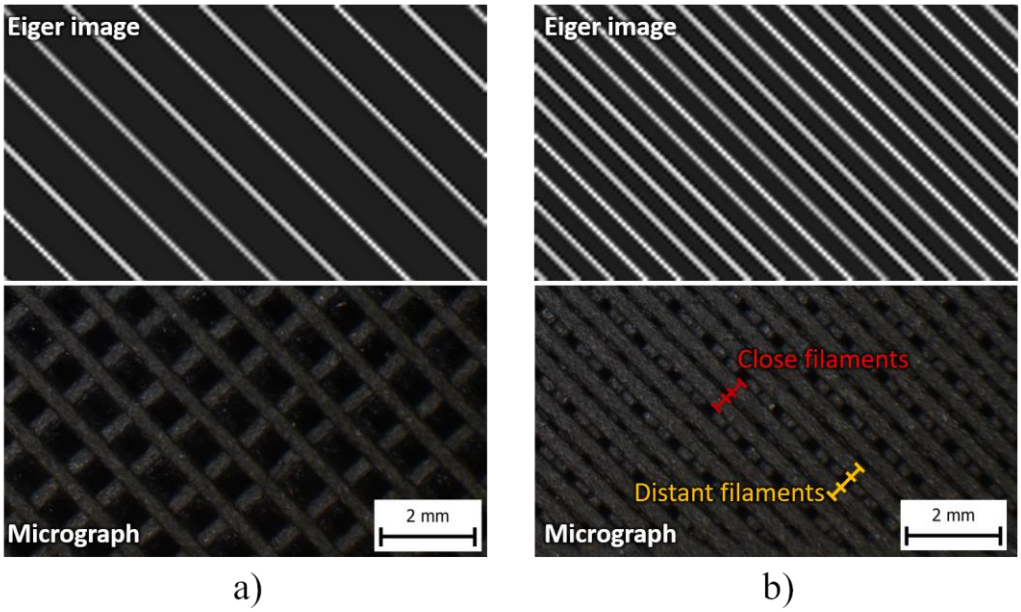

Fig. 7: Comparison between actual specimens and images generated by Eiger for the a) R40 and b) R80 patterns (same scale)

A geometrical simplification was also made for the rectangular infills. Fig. 8 shows both the shell and the solid models of the R40 infill. As shown, the infill is modelled considering the cell boundaries as continuous walls, like for the hexagonal and triangular case (see Fig. 6). For these two cases, the printer creates physically closed cells; however, this is not true for the rectangular infill: the alternating filament deposition in the latter case creates empty spaces that are not considered in the modelling. This is schematically depicted in Fig. 9. There will thus be an underestimation of the actual porosity in the rectangular pattern.

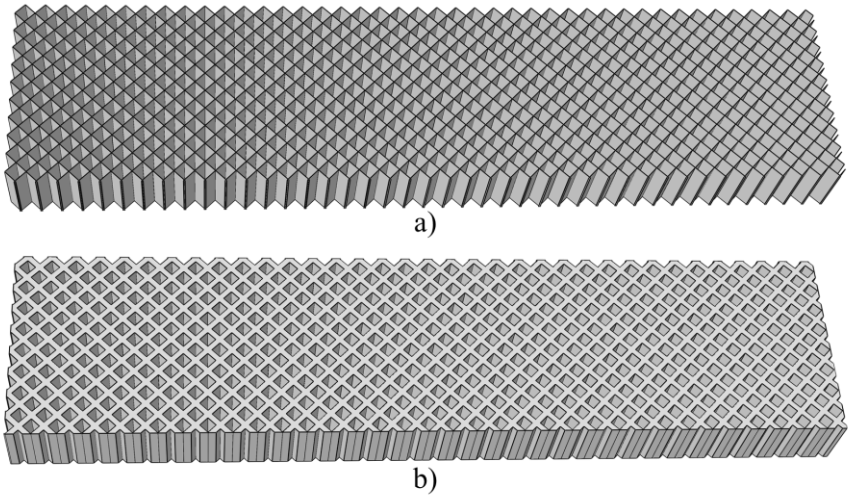

Fig. 8: a) Shell and b) solid model of the R40 infill

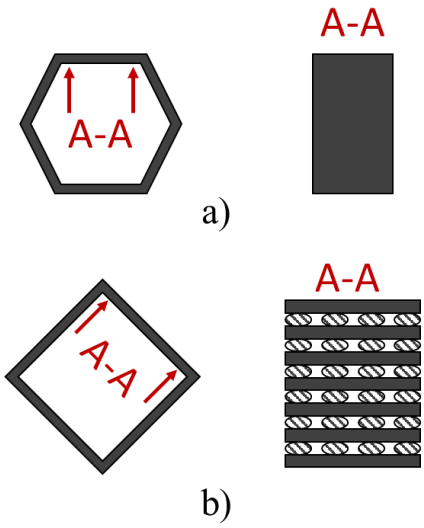

Fig. 9: Geometry of the a) hexagonal and b) rectangular cells. Note how in the hexagonal case, the cells walls are actually continuous, while the walls of the rectangular pattern are made of overlapping filaments

For the shell modelling, it was possible to mesh all infills using quadrangular elements. The orientations were assigned using the local normals of the shell elements. For the solid modelling, a hex-dominated mesh was used. Local orientations were assigned to the hexagonal and triangular cells by partitioning the cells into sub-cells and assigning the orientations to these sub-cells individually. Fig. 10 shows this for both cases, at 40% infill. Due to significantly smaller cells for the rectangular case (see Fig. 8b or Fig. 13), it was decided to not partition them for the orientation assignment. Instead, axis 1 and 2 of the material coordinate system

were oriented at ±45°, along the two filaments' directions, and the longitudinal Onyx Young's modulus was assigned along both axes. For all simulations, the global element length was set to 0.4 mm (equal to the filament width), while a number of 8 elements through the specimens' thickness was imposed. Fig. 11 showcases the H40 shell and solid meshes to illustrate this meshing strategy.

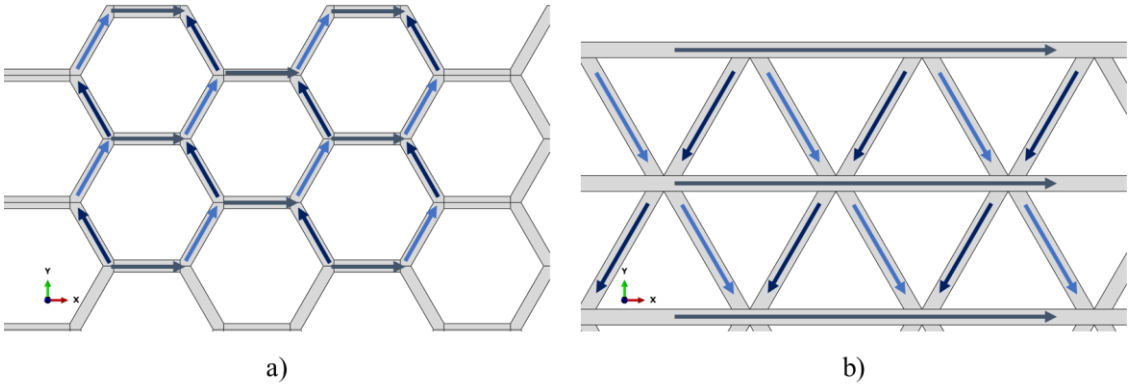

Fig. 10: Orientation assignment for the a) hexagonal and b) triangular cells. The arrows indicate the direction of axis-1, while the different colors highlights the splitting into different sub-cells.

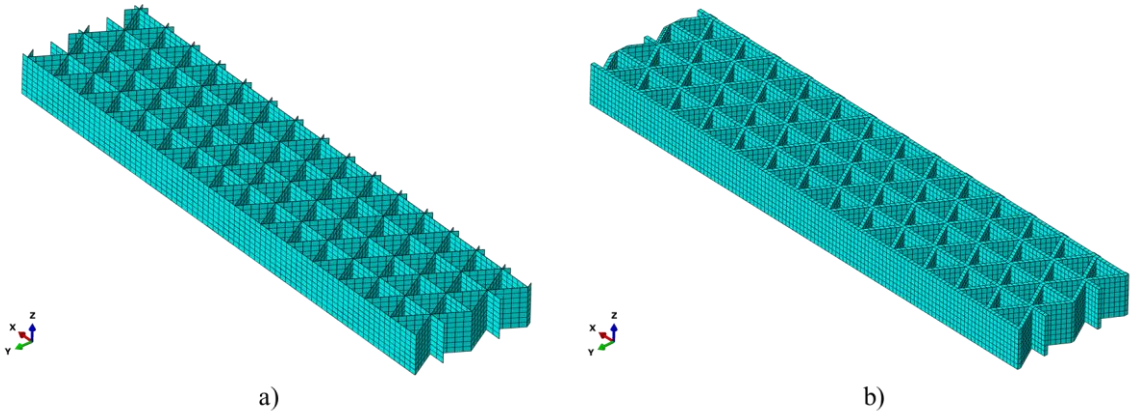

Fig. 11: a) Shell and b) solid mesh of the triangular core.

4.2 Simulation results

The rigidities obtained by FE simulations are reported in Table 6. The results of the tests and simulations are compared in Fig. 12. Almost all simulations allowed for the specimens' stiffness to be evaluated with a maximum difference of 15% with respect to experimental tests. A larger difference is observed for the R60 and R80 specimens: the solid simulation overpredicted the stiffness of the R60 by 19%, while a 20% and 25% overprediction was obtained for the R80 shell and solid simulations, respectively. These shell simulations leading to inaccurate predictions are based on the nominal dimensions provided by the Eiger software.

Table 6: Simulation results in terms of specimens' stiffness. ND and RD stand for Nominal Dimensions and Real Dimensions, respectively.

Infill	Hexagonal	Triangular	Rectangular
40 %	Shell: 13.4 N/mm	Shell: 15.5 N/mm	Shell: 16.1 N/mm
40 %	Solid: 14.1 N/mm	Solid: 15.8 N/mm	Solid: 15.9 N/mm
60 %	Shell: 13.6 N/mm	Shell: 15.6 N/mm	Shell: 17.9 N/mm
60 %	Solid: 14.5 N/mm	Solid: 16.6 N/mm	Solid: 20.2 N/mm
80 %	Shell: 13.6 N/mm	Shell: 17.3 N/mm	Shell (ND): 20.7 N/mm Shell (RD): 17.7 N/mm
80 %	Solid: 14.8 N/mm	Solid: 16.2 N/mm	Solid: 21.5 N/mm

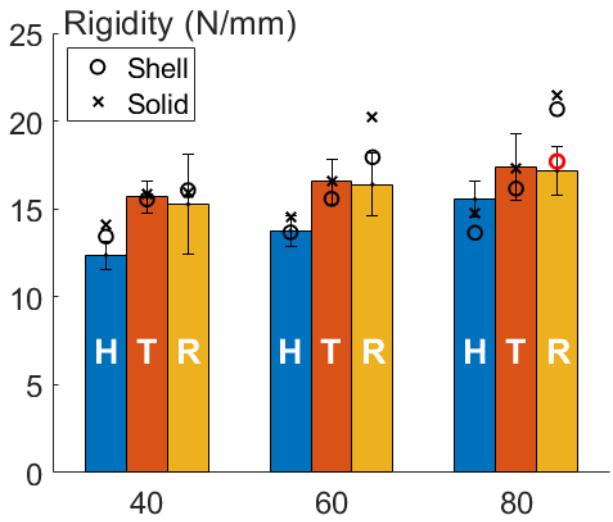

Fig. 12: Comparison of tests and simulations predicted stiffness. The red circle refers to the shell simulation using the true dimensions measured from the micrograph

The overpredictions in the rectangular infill simulations are likely due to an inaccurate geometrical description. Fig. 13b showcases the solid model of the R80 infill. Even considering the real dimensions of the infill, the model seems unfit for representing the real structure of the infill. As mentioned before, the filaments composing the rectangular infill are approximated as continuous walls, with a consequent underestimation of porosity, a detrimental factor for the performance of 3D printed materials [32]. Moreover, the square holes composing the cells have smaller edge length than the filament width. As a result, the modelled infill is more like a solid block than the actual infill structure. Fig. 13a showcases the solid model of the R60 infill. In this case, a cell-based structure is more recognisable, but the geometrical approximation is likely to still have an impact on the overpredicted stiffness. For this pattern, the edge of the square holes are 0.35 mm long, which is close to the 0.4 mm of the filament width. On the other hand, the approximation seems to have negligible effects on the R40 simulation (whose infill is shown in Fig. 8b). In this case, the square holes edges are 0.8 mm long, twice the filament width. Therefore, it seems that the solid modelling tends to overpredict the actual stiffness of the specimens when the length of the holes' edges approaches that of the filament width.

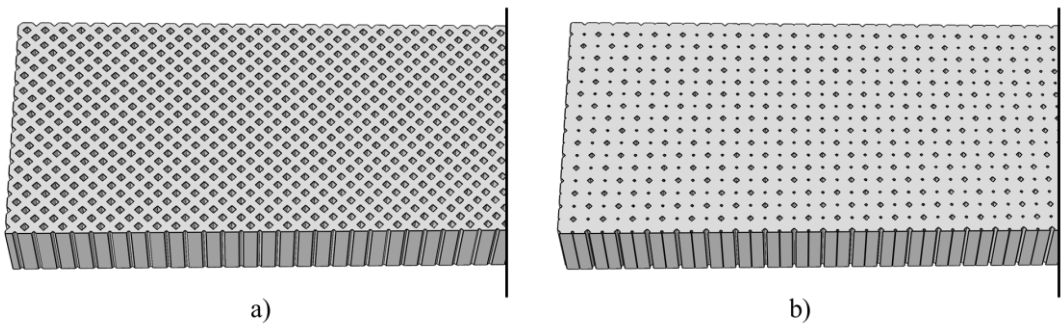

Fig. 13: The solid models of the a) R60 and of the b) R80 infill (only left half is shown)

The R80 shell simulation considering the real dimensions measured from the micrograph (the red circle in Fig. 12) lead to a significant improvement of the R80 shell model accuracy. This suggests that the stiffness overprediction of the R80 shell model originates mainly from the

difference between the nominal and real dimensions of the infill. For the shell models, the geometrical approximation of the filaments as continuous walls and the consequent porosity underestimation thus seems to have minor effects.

It is worth noting that, for the hexagonal and triangular simulations, the FE model allowed to estimate an increase of stiffness always less than 5% when increasing the infill parameter. While this is acceptable for the triangular infill cases (see Table 5), it is half of the measured change for the hexagonal case. As a result, the H40 and the H80 stiffnesses are slightly underpredicted and overpredicted, respectively. This raises doubts about the validity of these modelling techniques for hexagonal patterns with infill percentage outside the tested range. A higher rate of change was predicted by the model for the rectangular case; however, due to the aforementioned inaccuracies, the rate of change of his case will not be discussed further.

4.3 Discussion on modelling strategies

Overall, none of the modelling technique applied in this work can be considered better than the other. The most accurate results were obtained by one or another, according to the different case considered. The shell modelling technique was less affected by the differences between the nominal and the actual infill geometry found for the 60% and 80% infill with rectangular pattern. On the other hand, the solid model proved to be more accurate for the triangular case. For the hexagonal case, both shell and solid models lead to overall similar differences from the experimental results. The correct modelling approach thus needs to be selected case by case. Both approaches should be carefully considered in case of blind predictions, especially at high infill parameters.

The tested approaches can be useful in designing simple 3D printed parts, especially in the selection of the infill shape and density. The infills' geometries were modelled using the Eiger slicer software, that showed significant differences from the actual printed geometry only for the R80 specimens. This is of particular industrial interest, since it makes it possible to evaluate the

stiffness of a part before printing it. However, both modelling approaches rely on an explicit representation of the specimens' infill. Despite all simulations required only few minutes of computational time, such infill representation makes the pre-processing phase more complex. This makes both approaches hardly applicable to more complex geometries or structures. A more efficient and accurate modelling of sandwich-like 3D printed structures would probably require an implicit representation of the infill. Homogenisation techniques for the core (see [33]), or even for both the core and the skins, would allow such representation and significantly simplify the FE analysis of complex 3D printed parts. However, difficulties may be expected, because significant variations of both stiffness and strength may be occur between core, contour and skins [33]. Future work will focus on this topic and would profit from the experience gained in modelling the infills, a step which is fundamental for an efficient homogenization of the elastic properties.

5 Conclusions

This work has investigated the effects of different infill shapes and densities on the flexural, elastic performance of 3D printed specimens designed like a sandwich structure, as well as the different techniques to model their flexural behaviour.

Several specimens were manufactured with three different infill shape patterns: hexagonal, triangular and rectangular. Moreover, three different infill parameters were considered for each shape: 40%, 60% and 80%. These specimens were tested under three points bending conditions. The stiffness of the hexagonal specimens was between 13% and 25% lower than the triangular and rectangular specimens, that instead showed similar performance. The infill density had a linear effect on the flexural stiffness, with higher rigidities obtained at higher infill parameters. This confirmed the non-negligible role of the stiffness of the infill on the flexural behaviour of sandwich-like structures.

To predict the specimen's stiffness, preliminary tensile tests were performed on 100% infill specimens with different printing orientation. The Onyx lamina elastic properties were thus back calculated from these tests. The longitudinal modulus identified on printed specimens differed significantly form the value reported in the supplier's data sheet, thus confirming the importance of accounting for the effects of the manufacturing process on the material's elastic properties. The method proposed in this work for the identification of the elastic constants allowed for the sandwich specimens to be modelled. The good agreement between the values of the bending stiffness estimated by FE analysis and those measured experimentally implicitly confirms the validity of the method.

For the three points bending simulations, both shell and solid modelling of the infill were considered. Both approaches lead to accurate stiffness predictions for the triangular and hexagonal infills; however, the stiffness increase due to an infill percentage increase of the latter case was significantly underestimated. This may give rise to doubts about the effectiveness of the considered modelling approaches for hexagonal infill percentage outside the considered range. While providing good prediction for the 40% rectangular infill, both approaches led to significant stiffness overpredictions in the other two rectangular specimens. The reasons for such inaccuracies were attributed to an inaccurate description of the real geometry of the infill at high infill densities.

This work contributes to clarify the effects of the infill shape and density on the bending performance of additively manufactured sandwich-like composites. It also suggests to designers a useful modelling approach that can be applied before the actual printing of the part. Moreover, it suggests what modelling approach to consider, according to the part's infill geometry and density. It finally highlights the need for homogenisation-based modelling technique for the FE analysis of more complex 3D printed structures.

6 Ackonwledgments

Support by the Italian Ministry for Education, University and Research through the project Department of Excellence LIS4.0 (Integrated Laboratory for Lightweight e Smart Structures) is acknowledged.

7 References

[1] El Moumen A, Tarfaoui M, Lafdi K. Additive manufacturing of polymer composites: Processing and modeling approaches. Compos Part B Eng 2019;171:166–82.

[2] Huang SH, Liu P, Mokasdar A, Hou L. Additive manufacturing and its societal impact: a literature review. Int J Adv Manuf Technol 2013;67:1191–203.

[3] Parandoush P, Lin D. A review on additive manufacturing of polymer-fiber composites. Compos Struct 2017;182:36–53.

[4] Dizon JRC, Espera AH, Chen Q, Advincula RC. Mechanical characterization of 3D-printed polymers. Addit Manuf 2018;20:44–67.

[5] Ahn SH, Montero M, Odell D, Roundy S, Wright PK. Anisotropic material properties of fused deposition modeling ABS. Rapid Prototyp J 2002;8:248–57.

[6] Chacón JM, Caminero MA, García-Plaza E, Núñez PJ. Additive manufacturing of PLA structures using fused deposition modelling: Effect of process parameters on mechanical properties and their optimal selection. Mater Des 2017;124:143–57.

[7] Casavola C, Cazzato A, Moramarco V, Pappalettere C. Orthotropic mechanical properties of fused deposition modelling parts described by classical laminate theory. Mater Des 2016;90:453–8.

[8] Rankouhi B, Javadpour S, Delfanian F, Letcher T. Failure Analysis and Mechanical Characterization of 3D Printed ABS With Respect to Layer Thickness and Orientation. J Fail Anal Prev 2016;16:467–81.

[9] Carneiro OS, Silva AF, Gomes R. Fused deposition modeling with polypropylene. Mater Des 2015;83:768–76.

[10] Sood AK, Ohdar RK, Mahapatra SS. Parametric appraisal of mechanical property of fused deposition modelling processed parts. Mater Des 2010;31:287–95.

[11] Zhong W, Li F, Zhang Z, Song L, Li Z. Short fiber reinforced composites for fused deposition modeling. Mater Sci Eng A 2001;301:125–30.

[12] Tekinalp HL, Kunc V, Velez-Garcia GM, Duty CE, Love LJ, Naskar AK, et al. Highly oriented carbon fiber-polymer composites via additive manufacturing. Compos Sci Technol 2014;105:144–50.

[13] Ning F, Cong W, Qiu J, Wei J, Wang S. Additive manufacturing of carbon fiber reinforced thermoplastic composites using fused deposition modeling. Compos Part B Eng 2015;80:369–78.

[14] Jiang D, Smith DE. Anisotropic mechanical properties of oriented carbon fiber filled polymer composites produced with fused filament fabrication. Addit Manuf 2017;18:84–94.

[15] Ning F, Cong W, Hu Y, Wang H. Additive manufacturing of carbon fiber-reinforced plastic composites using fused deposition modeling: Effects of process parameters on tensile properties. J Compos Mater 2017;51:451–62.

[16] Naranjo-Lozada J, Ahuett-Garza H, Orta-Castañón P, Verbeeten WMH, Sáiz-González D. Tensile properties and failure behavior of chopped and continuous carbon fiber composites produced by additive manufacturing. Addit Manuf 2019;26:227–41.

[17] Papon EA, Haque A. Fracture toughness of additively manufactured carbon fiber reinforced composites. Addit Manuf 2019;26:41–52.

[18] Brenken B, Barocio E, Favaloro A, Kunc V, Pipes RB. Fused filament fabrication of fiber-reinforced polymers: A review. Addit Manuf 2018;21:1–16.

[19] Markforged. Onyx Datasheet 2020.

[20] Fernandez-Vicente M, Calle W, Ferrandiz S, Conejero A. Effect of Infill Parameters on Tensile Mechanical Behavior in Desktop 3D Printing. 3D Print Addit Manuf 2016;3:183–92.

[21] Li T, Wang L. Bending behavior of sandwich composite structures with tunable 3D-printed core materials. Compos Struct 2017;175:46–57.

[22] Gibson LJ, Ashby MF. Cellular Solids: Structure and Properties. 2nd ed. Cambridge University Press; 1997.

[23] Tang H, Chen H, Sun Q, Chen Z, Yan W. Experimental and computational analysis of structure-property relationship in carbon fiber reinforced polymer composites fabricated by selective laser sintering. Compos Part B Eng 2021;204:108499.

[24] Raju B, Hiremath SR, Roy Mahapatra D. A review of micromechanics based models for effective elastic properties of reinforced polymer matrix composites. Compos Struct 2018;204:607–19. https://doi.org/10.1016/j.compstruct.2018.07.125.

[25] Choi JY, Kortschot MT. Stiffness prediction of 3D printed fiber-reinforced thermoplastic composites. Rapid Prototyp J 2019;26:549–55.

[26] EN ISO 527-4. Determination of tensile properties. 1997.

[27] 178 ISO. Plastics — Determination of flexural properties. 2019.

[28] Barbero EJ. Introduction to Composite Materials Design. II Edition. Boca Raton (FL, US): CRC Press; 2011.

[29] Narula SC, Wellington JF. Prediction, Linear Regression and the Minimum Sum of Relative Errors. Technometrics 1977;19:185–90.

[30] Gholamy A, Kreinovich V. How to use absolute-error-minimizing software to minimize relative error: practitioner's guide. Int Math Forum 2017;12:763–70.

[31] Abràmoff MD, Magalhães PJ, Ram SJ. Image processing with imageJ. Biophotonics Int 2004;11:36–41.

[32] Yeole P, Hassen AA, Kim S, Lindahl J, Kunc V, Franc A, et al. Mechanical Characterization of High-Temperature Carbon Fiber-Polyphenylene Sulfide Composites for Large Area Extrusion Deposition Additive Manufacturing. Addit Manuf 2020;34:101255.

[33] Dialami N, Chiumenti M, Cervera M, Rossi R, Chasco U, Domingo M. Numerical and

experimental analysis of the structural performance of AM components built by fused filament fabrication. Int J Mech Mater Des 2020.